Signature of chiral anomaly in the Weyl semimetal $TaRhTe_4$

M. Behnami,[1,2,3] D. V. Efremov,[1] S. Aswartham,[1] G. Shipunov,[1] B. R. Piening,[1] C. G. F. Blum,[1] V. Kocsis,[1] J. Dufouleur,[1] I. Pallecchi,[4] M. Putti,[3,4] B. Büchner,[1,2] H. Reichlova,[1,2,5] and F. Caglieris[4,*]

[1]*IFW Dresden, P. O. Box 270116, 01171 Dresden, Germany*

[2]*Institut für Festkörper- und Materialphysik, Technische Universität Dresden, 01062 Dresden, Germany*

[3]*Department of Physics, University of Genoa, 16146 Genova, Italy*

[4]*CNR-SPIN, 16152 Genova, Italy*

[5]*Institute of Physics ASCR, v. v. i., Cukrovarnická 10, 16253, Praha 6, Czech Republic*

(Received 13 December 2024; revised 29 May 2025; accepted 11 June 2025; published 1 July 2025)

$TaRhTe_4$ is a type-II Weyl semimetal (WSM), exhibiting four Weyl points in proximity to the Fermi level. In this article, we report our results of a systematic study of longitudinal magnetoresistance (MR) in $TaRhTe_4$. Our findings indicate that MR becomes negative only when the magnetic field is applied parallel to the electric field. By rotating **E** (as well as **B**), we show that its origin is consistent with the prediction of the chiral anomaly, while the current jetting effect and weak localization could be excluded. The negative MR persists up to room temperature, suggesting that $TaRhTe_4$ exhibits distinctive properties within the family of WSMs.

DOI: 10.1103/n7lw-7xqj

I. INTRODUCTION

In the last decade, tremendous attention has been devoted to the study of Weyl and Dirac semimetals (DSMs). These are classes of topological materials hosting relativistic quasiparticles named Weyl and Dirac fermions [1,2]. The electronic band structure of these materials is characterized by band-touching points, identified as Weyl and Dirac points, respectively, and linear quasiparticle dispersion in proximity to these points [3].

In three-dimensional (3D) DSMs, both inversion symmetry (IS) and time-reversal symmetry (TRS) are present, making Dirac cones fourfold degenerate. In contrast, in Weyl semimetals (WSMs), either TRS or IS is broken, which results in Weyl points (WPs) being nondegenerate and described by a topological charge. The topological nature of WPs leads to many interesting properties, including their protection against small perturbations and distortions [3]. In addition, WSMs show many interesting phenomena, which can be observed experimentally. One of those is the development of protected surface states, called Fermi arcs, which can be identified through angle-resolved photoemission spectroscopy and represent the fingerprint of the Weyl cones in the bulk [4]. Another effect predicted in WSMs is the chiral anomaly, which is characterized by the anomalous nonconservation of a chiral current [5–10].

The chiral anomaly manifests itself in transport properties as a negative contribution to the longitudinal magnetoresistance (MR) when the applied magnetic field is parallel to the electric field that causes the motion of the carriers [11,12]. Figure 1(a) shows a schematic representation of this effect. Such phenomenology has been observed in several WSMs, including NbP, NbAs [7,9], and DSMs $ZrTe_5$ [10], Na_3Bi [13], Cd_3As_2 [14], and GdPtBi [15,16]. In all of these cases, numerous WPs are close to the Fermi level, making it difficult to attribute the effect to any specific couple of WPs.

Here, we study $TaRhTe_4$, a sibling compound of $TaIrTe_4$, which is the simplest example of a WSM, often referred to as the *hydrogen atom* in the world of WSMs due to its minimal number of WPs near the Fermi level, which must be four for noncentrosymmetric WSMs [17–19]. $TaIrTe_4$ has many interesting properties, from the points of view of both fundamental physics and next-generation electronics. For instance, it shows strong positive MR at low temperatures [17], presents the room-temperature nonlinear Hall effect [20], surface superconductivity [21], and anisotropic photoresponse [22,23]. $TaRhTe_4$ is much less investigated [24,25].

$TaRhTe_4$ crystallizes in the same orthorhombic noncentrosymmetric space group (No: $Pmn2_1$) structure as $TaIrTe_4$, and it is a layered van der Waals (vdW) material. The crystal structure can be derived from WTe_2 [26], as shown in Fig. 1(b).

In this article, we report our systematic investigation of the magnetotransport properties of a $TaRhTe_4$ single crystal. We measured the MR signal by applying a magnetic field up to 10 T in various geometries, including in-plane (parallel and perpendicular to the electric field) and out-of-plane (perpendicular to the electric field). Surprisingly, the magnetotransport properties of $TaRhTe_4$ strongly differ from $TaIrTe_4$ (shown in Fig. S1 in the Supplemental Material [27]) despite the similarity of the crystal and electronic band structures [26]. In the $TaRhTe_4$ sample, we observe a negative MR when the electric and magnetic fields are parallel to each other, either oriented along the crystallographic *a* or *b* direction. Furthermore, this negative MR persists up to room temperature, suggesting that $TaRhTe_4$ possesses unique properties within the family of WSMs.

*Contact author: federico.caglieris@spin.cnr.it

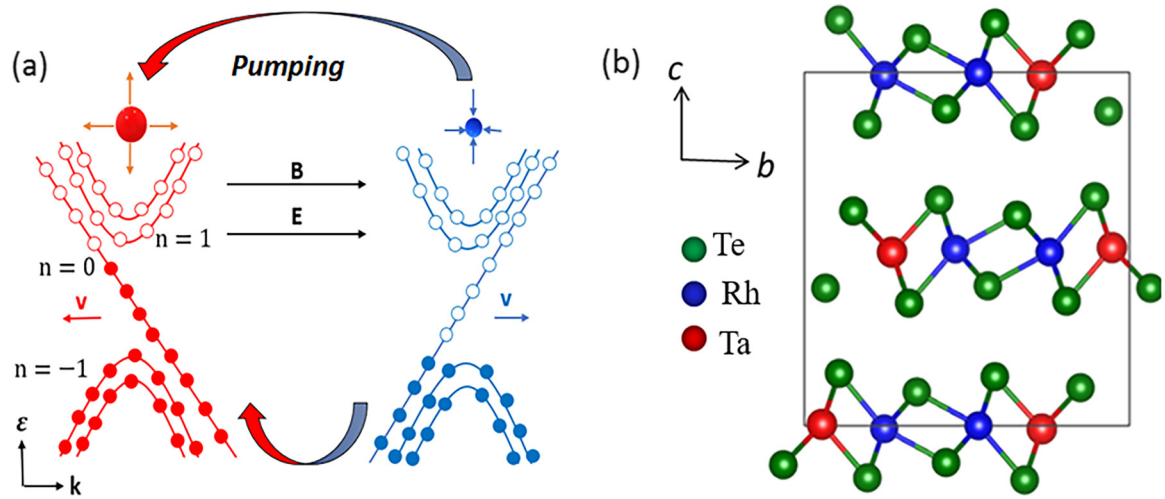

FIG. 1. (a) Schematic illustration of bulk Landau levels of a pair of Weyl points. The linear lines represent the zeroth quantum Landau level with blue and red chiralities in a **B** ∥ **E**. (b) Crystal structure of the $TaRhTe_4$ compound.

II. EXPERIMENTAL

The single crystals were grown using the self-flux method. To prepare the crystals for further study, the surfaces, which were contaminated by a small amount of flux, were mechanically cleaved [26]. The orientation of the crystal axis has been systematically determined by x-ray Laue diffraction.

The setup for DC electric transport measurements was prepared by gluing the electrodes (silver wires 50 μm thick) to the samples using silver paint (Dupont 4929N), as shown in the inset Fig. 2(a). All transport measurements were carried out within a temperature range from 8 K to room temperature, using a tested homemade probe and Oxford cryostats equipped with sufficiently large magnets. A Keithley Standard Series 2400 Source Measure Unit (SMU) was used to apply the electric current, while a Keithley Nanovoltmeter Model 2182A was utilized to measure the voltage signal. A semisum of the data points acquired with positive and negative electric

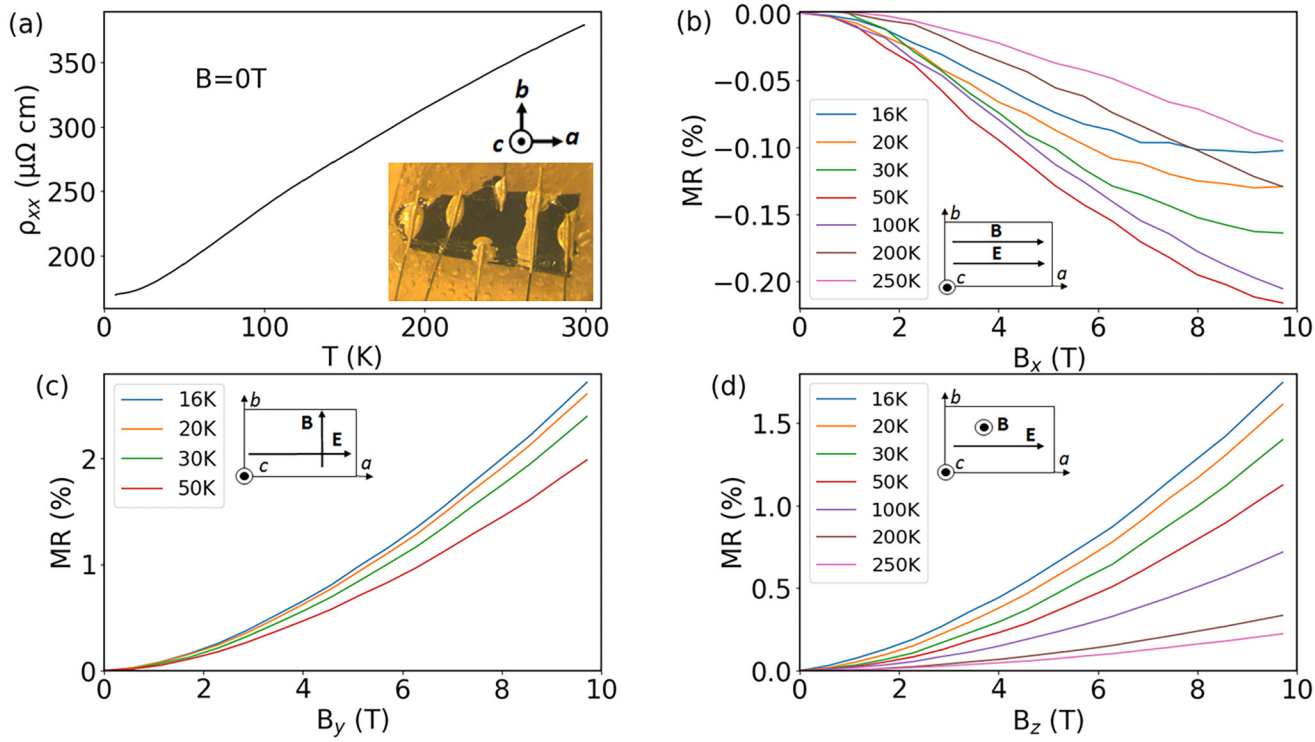

FIG. 2. Longitudinal magnetoresistance (MR) in the first sample of $TaRhTe_4$. (a) Temperature dependence of resistivity. Inset: Image of our first $TaRhTe_4$ single crystal prepared for electric measurement. (b) Longitudinal MR in the case of an in-plane magnetic field with **B** ∥ **E**. (c) Longitudinal MR in the case of an in-plane magnetic field with **B** ⊥ **E**. (d) Longitudinal MR in the case of out-of-plane magnetic field with **B** ⊥ **E**.

currents has been systematically performed in all the measurements to eliminate the thermoelectric background.

The MR was measured in magnetic field up to 10 T, applied both in-plane (parallel and perpendicular to the electric field) and out-of-plane (perpendicular to the electric field).

III. RESULTS

Figure 2 shows the magnetotransport measurements for the first sample of $TaRhTe_4$. More in detail, Fig. 2(a) presents the temperature dependence of the electrical resistivity in zero magnetic field. The curve shows metallic behavior decreasing monotonically with the temperature and a moderate residual-resistivity ratio (RRR) = 2.23. Figures 2(b)–2(d) show the dependence of resistivity on the magnetic field. In this experiment, the electric current was injected along the crystallographic *a* axis, and as a consequence, the electric field results oriented along the same axis. The magnetic field was applied sequentially along all three crystallographic axes, as shown in the inset of Fig. 2(a). The presented MR is defined as $\mathrm{MR} = 100 \times \frac{\rho(\mathbf{B})-\rho(0)}{\rho(0)}$, where $\rho(\mathbf{B})$ and $\rho(0)$ are the resistivities of the sample in a magnetic field **B** and in zero magnetic field, respectively.

Figure 2(b) shows the resistivity as a function of the magnetic field (**B**), where **B** is in the *ab* plane and parallel to **E**. The MR is negative over the whole range of studied temperatures. However, at $T = 200$ and 250 K, the curves exhibit a parabolic shape up to 10 T, while for $T \leqslant 100$ K, $\mathrm{MR} \sim \mathbf{B}^2$ only in the low-field region and a change of concavity with a tendency to an upturn occurs at high fields. At $T = 50$ K and $\mathbf{B} = 10$ T, a negative MR of 0.21% is obtained. The measured behavior is very similar to that observed in NbP [9] and Cd_3As_2 [14]. Interestingly, the sibling compound $TaIrTe_4$ does not present any negative MR, as shown in Fig. S1 in the Supplemental Material [27].

Figures 2(c) and 2(d) present the MR as a function of the magnetic field applied along the crystal *b* and *c* axes, respectively. In both cases, MR is always positive and relatively small, reaching the maximum value of a few percent. In addition, it presents a parabolic behavior, which is indicative of the cyclotronic origin of the magnetoresistive effect [14].

To confirm the negative MR observed in Fig. 2(b), we deeply investigated a second sample. To this aim, we chose a slab-shaped sample of $TaRhTe_4$, and we attached six electrodes on top of that, which enabled us to measure the MR signal along different crystallography axes (see inset of Fig. 3). We first measured the zero-field resistivity of the second sample in different configurations, as shown in Fig. 3. Interestingly, the resistivity estimated with voltage electrodes along the *a* axis (V_{26} and V_{35}) and current prevalently injected along the *a* axis is relatively different with respect to the resistivity evaluated putting both voltage and current electrodes along the sample *b* axis (I_{34} and V_{56}). The different RRR values (2.68, 2.55, and 1.44) indicate the relative anisotropy between the *a*- and *b*-axis conductivities. From the finite element simulations (see Fig. S2 in the Supplemental Material [27]) and comparison of the experimental values of zero-field resistances measured in the three configurations, we extracted the value of in-plane resistivity anisotropy $\rho_b/\rho_a = 6.8$.

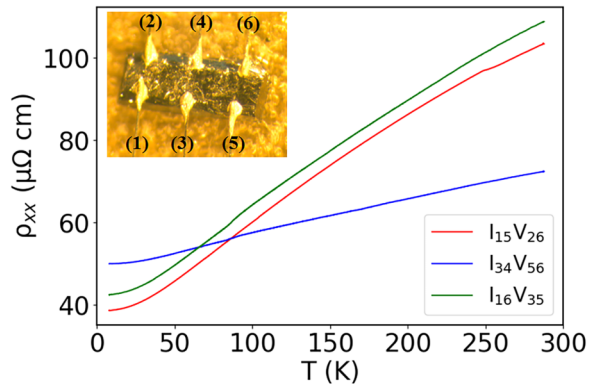

FIG. 3. Temperature dependence of resistivity for three configurations of the second sample of $TaRhTe_4$. Inset: Picture of the second sample of $TaRhTe_4$. The numbers indicate the electrodes that we used to apply the electric current and measure the voltage.

After a zero-field characterization, we measured the sample MR. For this specimen, we explored the following configurations.

A. Magnetic field in the *ab* plane and electric field parallel to the *a* axis of the crystal

In the first setup, we injected current from contact (1) to contact (5) and measured the voltage signal between contacts (2) and (6), with the magnetic field applied parallel to the *a* axis of the crystal. As illustrated in Fig. 4(a), we observed a negative MR, which reaches the maximum value of 0.22% and persists up to high temperatures. In the second setup, we changed the direction of the magnetic field from parallel to perpendicular to the *a* axis. This time, we observed a positive MR which reached 3.9% for $T = 9$ K and $\mathbf{B} = 10$ T, as depicted in Fig. 4(d).

B. Magnetic field in the *ab* plane and electric field parallel to the *b* axis of the crystal

In this configuration, we injected current from contact (3) to contact (4) and measured the voltage signal between contacts (5) and (6). First, we applied a magnetic field parallel to the *b* axis of the crystal, observing again a negative MR (up to 0.19%), as illustrated in Fig. 4(b). Secondly, we changed the direction of the magnetic field from parallel to perpendicular to the sample *b* axis. This time, we observed a positive MR up to 4.2% at $T = 9$ K and $\mathbf{B} = 10$ T, as depicted in Fig. 4(e).

C. Magnetic field in the *ab* plane and electric field at 30° from the *a* axis of the crystal

In the third configuration, we injected current from contact (1) to contact (6) and measured the voltage signal between contacts (3) and (5). In the first experiment, we applied a magnetic field parallel to both an electric field and the diagonal axis of the sample, tilted about 30° from the *a* axis. Clearly, such an angle is only a nominal value, not necessarily corresponding to the exact direction of the electric field, which strictly depends on the actual current path. As illustrated in Fig. 4(c), we observed a positive MR. At $T = 8$ K and $\mathbf{B} = 10$ T, the highest positive MR of 0.45% can be obtained.

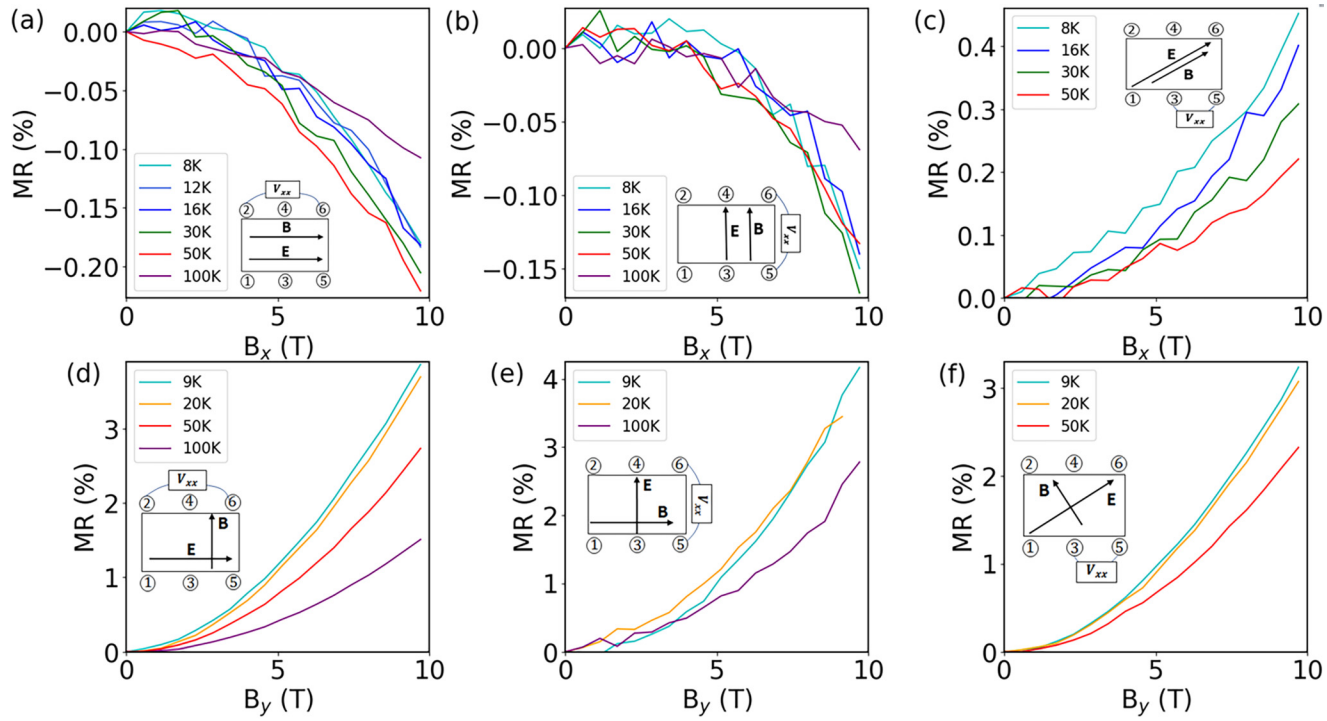

FIG. 4. Longitudinal magnetoresistance (MR) in the second sample of $TaRhTe_4$. (a)–(c) Longitudinal MR in the case of an in-plane magnetic field with $\mathbf{B} \parallel \mathbf{E}$. The applied magnetic field is along a, b, and 30° from the a axis of the crystal, respectively. (d)–(f) Longitudinal MR in the case of an in-plane magnetic field with $\mathbf{B} \perp \mathbf{E}$. The applied magnetic field is along b, a, and 30° from the b axis of the crystal, respectively.

In the second configuration, we changed the direction of the magnetic field from parallel to perpendicular and measured the signal. Once again, we observed a positive MR, as depicted in Fig. 4(f). At $T = 9$ K and $\mathbf{B} = 10$ T, a positive MR of 3.2% was measured. Therefore, we did not observe negative MR in this setup, whether the magnetic field was parallel or perpendicular.

IV. DISCUSSION

In nonmagnetic conductors, the presence of external magnetic fields typically generates a magnetoresistive effect caused by the cyclotronic motion of the charge carriers, when the field itself has a component perpendicular to the direction of the current density vector [14]. Such a semiclassical effect strongly depends on both intrinsic and extrinsic properties of the measured sample, such as the effective mass of the charge carriers and the scattering time and, in the low-field limit, is proportional to B^2. In general, clean systems exhibit higher cyclotronic MR, intuitively depending on the number of cyclotronic orbits traveled by charge carriers between a scattering event and the following one. As expected, in our case, this is also the dominant contribution in all the configurations with the magnetic and electric fields not aligned in the same direction.

In WSMs, an additional negative contribution to the MR is possibly caused by the chiral anomaly. Equivalently, the chiral anomaly manifests itself as a positive contribution to the electrical conductivity in magnetic field [11,28], only when it is parallel to the electric field that causes the motion of charge carriers, namely, to the direction of the injected current. In this situation, the correction to the electrical conductivity due to the chiral anomaly for a type-I WSM reads [11]

$$\Delta\sigma(B) = \frac{e^2}{4\pi^2\hbar c}\frac{v_F}{c}\frac{(eBv_F)^2}{\epsilon_F^2}\tau_a, \tag{1}$$

where τ_a^{-1} is the longitudinal axial current relaxation rate, c is the light speed, and ϵ_F and v_F are the Fermi energy and the Fermi velocity, respectively. Remarkably, it has been demonstrated that the quadratic-in-field dependence holds also in the case of type-II or tilted WSMs, for which a positive longitudinal magneto-conductivity appears for all finite angles between the tilt direction of the cones and the direction of the applied magnetic/electric field [29]. Figure 5 presents the positive magnetoconductivity of the first sample of $TaRhTe_4$ in the experimental configuration of Fig. 2(b). All the curves are nicely reproduced by the $\mathbf{B}^2$ fitting function, corroborating the chiral anomaly as a possible source for the observed effect. Here, $\Delta\sigma = \sigma(\mathbf{B}) - \sigma(\mathbf{B} = 0)$, where $\sigma(\mathbf{B})$ and $\sigma(\mathbf{B} = \mathbf{0})$ are the conductivity of the first sample in a magnetic field and in zero magnetic field, respectively. The same result is obtained for the second sample as shown in Figs. S3 and S4 in the Supplemental Material [27].

In the following, we will briefly discuss other possible sources of negative MR in nonmagnetic materials. The first possible phenomenon that can cause negative MR is the weak localization effect [30–32]. However, weak localization is typically observed in two-dimensional (2D) or highly anisotropic (out-of-plane/in-plane anisotropy of electronic properties) materials, when the magnetic field is applied in

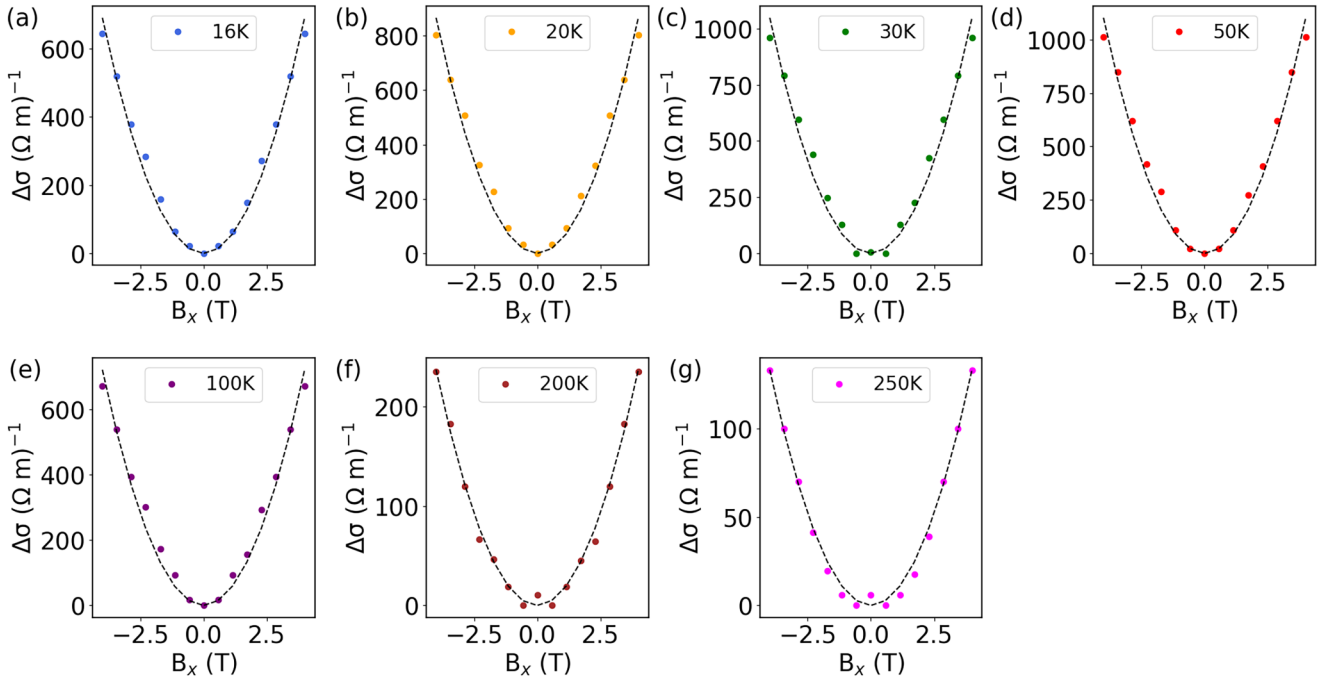

FIG. 5. Positive contribution of electrical conductivity as a function of magnetic field for the first sample of $TaRhTe_4$. The direction of a magnetic field is parallel to the electric field (**B** ∥ **E**).

the out-of-plane direction. In this condition, the threading of magnetic flux in interfering current paths may result in negative MR. In our case, the negative MR appears when the field and current are both in-plane and parallel to each other, which is the configuration that minimizes the threading of magnetic flux in interfering current paths. Moreover, both the magnitude and the magnetic field dependence of our MR are not described by conventional models for weak localization (see Supplemental Material [27]).

The main alternative to the chiral anomaly to explain the observed phenomenology is represented by the so-called current jetting effect, which appears as a semiclassical negative longitudinal MR caused by a nonuniform current distribution in the sample when **B** ∥ **E**. Such an effect typically appears when current contacts are smaller than the cross-section of the sample, causing field-induced steering of the current to the direction of the magnetic field [16,33]. In the measurement configuration of Fig. 2(b), referring to sample one, the size of the current electrodes is comparable with the sample width [see inset of Fig. 2(a)]. Therefore, we do not expect any substantial current jetting. Remarkably, in the case of sample two, where the electrodes are smaller and differently distributed across the sample (see inset of Fig. 3), the experimental configurations in Figs. 4(a) and 4(b) return almost the same value of negative MR, very similar to the one observed in sample one. In addition, we tested the influence of size and position of the electrical contacts on the appearance of the negative MR by measuring several other samples. In all the experiments, we verified that the only relevant parameter is the mutual orientation of current, magnetic field, and crystal axis, which must be parallel to each other, as expected in case of chiral anomaly (see Supplementary Material [27]).

Finally, we note that, in sample one, at $T < 100$ K, the negative magnetoresistive curves of Fig. 2(b) change their concavity, with a tendency to turn up at high fields. This effect can be trivially explained through an involuntary tilting of the applied magnetic field toward the out-of-plane direction, which causes an additional positive cyclotronic component that becomes dominant for sufficiently large fields. This spurious effect also accounts for the nonmonotonic trend in temperature of the curves in Fig. 2(b). The curves a $T = 200$ and 250 K do not show the upturn due to the strong suppression of the cyclotronic MR at high temperatures. Hence, the insensitivity of the observed MR to the geometry and distribution of the current electrodes on the sample excludes with reasonable certainty the current jetting as a possible source for the negative MR, in favor of an intrinsic phenomenon related to its nontrivial topology.

V. CONCLUSIONS

In conclusion, we have systematically measured the MR of two single crystals of $TaRhTe_4$, with different experimental configurations by varying both the distribution of the current/voltage electrodes across the samples and the applied magnetic field direction. In the setups where the applied electric and magnetic fields are parallel to each other and aligned either along the a or b axis, we always measured a negative MR (or positive magnetoconductance) compatible with a chiral anomaly effect. The robustness of the observed phenomenology with respect to the change of geometry in the current electrodes allowed us to exclude the current jetting as an alternative source for the effect.

ACKNOWLEDGMENTS

We would like to thank Tino Schreiner and Danny Baumann for their technical support. M.B. acknowledges

Forschungsstipendien für Doktorandinnen und Doktoranden, 2024 via Project No. 57694190 and the IFW Excellence Program 2018. S.A. acknowledges Deutsche Forschungsgemeinschaft (DFG) via Project No. 523/4-1. We would like to acknowledge the financial support provided by the DFG through Project No. 449494427. This work was supported by the DFG under Germany's Excellence Strategy through the Wurzburg-Dresden Cluster of Excellence on Complexity and Topology in Quantum Matter—ct.qmat (EXC 2147, Project ID No. 242021). The project was supported by the Leibniz Association through the Leibniz Competition.

B.B., D.V.E., H.R., F.C., and M.B. proposed the study. G.Sh., B.R.P., C.G.F.B., and S.A. prepared and characterized the samples. M.B., H.R., V.K., M.P., J.D., I.P., D.V.E., and F.C. designed the measurement setup, performed the experiments, and analyzed the data. I.P. performed the finite element simulations. B.B., H.R., and F.C. supervised the study. M.B., H.R., D.V.E., and F.C. wrote the manuscript with input from all authors.

The authors declare no conflict of interest.

DATA AVAILABILITY

The data that support the findings of this article are openly available [34].

[1] B. Yan and C. Felser, Topological materials: Weyl semimetals, Annu. Rev. Condens. Matter Phys. **8**, 337 (2017).

[2] M. Z. Hasan, S.-Y. Xu, I. Belopolski, and S.-M. Huang, Discovery of Weyl fermion semimetals and topological Fermi arc states, Annu. Rev. Condens. Matter Phys. **8**, 289 (2017).

[3] N. P. Armitage, E. J. Mele, and A. Vishwanath, Weyl and Dirac semimetals in three-dimensional solids, Rev. Mod. Phys. **90**, 015001 (2018).

[4] Z. K. Liu, L. X. Yang, Y. Sun, T. Zhang, H. Peng, H. F. Yang, C. Chen, Y. F. Zhang, Y. F. Guo, D. Prabhakaran *et al.*, Evolution of the Fermi surface of Weyl semimetals in the transition metal pnictide family, Nat. Mater. **15**, 27 (2016).

[5] H. B. Nielsen and M. Ninomiya, The Adler-Bell-Jackiw anomaly and Weyl fermions in a crystal, Phys. Lett. B **130**, 389 (1983).

[6] T. Bevan, A. Manninen, J. Cook, J. R. Hook, H. E. Hall, T. Vachaspati, and G. E. Volovik, Momentum creation by vortices in superfluid ^{3}He as a model of primordial baryogenesis, Nature (London) **386**, 689 (1997).

[7] Y. Li, Z. Wang, P. Li, X. Yang, Z. Shen, F. Sheng, X. Li, Y. Lu, Y. Zheng, and Z.-A. Xu, Negative magnetoresistance in Weyl semimetals NbAs and NbP: Intrinsic chiral anomaly and extrinsic effects, Front. Phys. **12**, 127205 (2017).

[8] X. Huang, L. Zhao, Y. Long, P. Wang, D. Chen, Z. Yang, H. Liang, M. Xue, H. Weng, Z. Fang *et al.*, Observation of the chiral-anomaly-induced negative magnetoresistance in 3D Weyl semimetal TaAs, Phys. Rev. X **5**, 031023 (2015).

[9] A. C. Niemann, J. Gooth, S.-C. Wu, S. Bäßler, P. Sergelius, R. Hühne, B. Rellinghaus, C. Shekhar, V. Süß, M. Schmidt *et al.*, Chiral magnetoresistance in the Weyl semimetal NbP, Sci. Rep. **7**, 43394 (2017).

[10] Q. Li, D. E. Kharzeev, C. Zhang, Y. Huang, I. Pletikosić, A. V. Fedorov, R. D. Zhong, J. A. Schneeloch, G. D. Gu, and T. Valla, Chiral magnetic effect in $ZrTe_5$, Nat. Phys. **12**, 550 (2016).

[11] D. T. Son and B. Z. Spivak, Chiral anomaly and classical negative magnetoresistance of Weyl metals, Phys. Rev. B **88**, 104412 (2013).

[12] A. A. Burkov, Chiral anomaly and diffusive magnetotransport in Weyl metals, Phys. Rev. Lett. **113**, 247203 (2014).

[13] J. Xiong, S. K. Kushwaha, T. Liang, J. W. Krizan, M. Hirschberger, W. Wang, R. J. Cava, and N. P. Ong, Evidence for the chiral anomaly in the Dirac semimetal Na_3Bi, Science **350**, 413 (2015).

[14] H. Li, H. He, H.-Z. Lu, H. Zhang, H. Liu, R. Ma, Z. Fan, S.-Q. Shen, and J. Wang, Negative magnetoresistance in Dirac semimetal Cd_3As_2, Nat. Commun. **7**, 10301 (2016).

[15] M. Hirschberger, S. Kushwaha, Z. Wang, Q. Gibson, S. Liang, C. A. Belvin, B. A. Bernevig, R. J. Cava, and N. P. Ong, The chiral anomaly and thermopower of Weyl fermions in the half-Heusler GdPtBi, Nat. Mater. **15**, 1161 (2016).

[16] S. Liang, J. Lin, S. Kushwaha, J. Xing, N. Ni, R. J. Cava, and N. P. Ong, Experimental tests of the chiral anomaly magnetoresistance in the Dirac-Weyl semimetals Na_3Bi and GdPtBi, Phys. Rev. X **8**, 031002 (2018).

[17] S. Khim, K. Koepernik, D. V. Efremov, J. Klotz, T. Förster, J. Wosnitza, M. I. Sturza, S. Wurmehl, C. Hess, J. van den Brink *et al.*, Magnetotransport and de Haas–van Alphen measurements in the type-II Weyl semimetal $TaIrTe_4$, Phys. Rev. B **94**, 165145 (2016).

[18] K. Koepernik, D. Kasinathan, D. V. Efremov, S. Khim, S. Borisenko, B. Büchner, and J. van den Brink, $TaIrTe_4$: A ternary type-II Weyl semimetal, Phys. Rev. B **93**, 201101(R) (2016).

[19] I. Belopolski, P. Yu, D. S. Sanchez, Y. Ishida, T.-R. Chang, S. S. Zhang, S.-Y. Xu, H. Zheng, G. Chang, G. Bian *et al.*, Signatures of a time-reversal symmetric Weyl semimetal with only four Weyl points, Nat. Commun. **8**, 942 (2017).

[20] D. Kumar, C.-H. Hsu, R. Sharma, T.-R. Chang, P. Yu, J. Wang, G. Eda, G. Liang, and H. Yang, Room-temperature nonlinear Hall effect and wireless radiofrequency rectification in Weyl semimetal $TaIrTe_4$, Nat. Nanotechnol. **16**, 421 (2021).

[21] Y. Xing, Z. Shao, J. Ge, J. Luo, J. Wang, Z. Zhu, J. Liu, Y. Wang, Z. Zhao, J. Yan *et al.*, Surface superconductivity in the type II Weyl semimetal $TaIrTe_4$, Natl. Sci. Rev. **7**, 579 (2020).

[22] J. Lai, Y. Liu, J. Ma, X. Zhuo, Y. Peng, W. Lu, Z. Liu, J. Chen, and D. Sun, Broadband anisotropic photoresponse of the "hydrogen atom" version type-II Weyl semimetal candidate $TaIrTe_4$, ACS Nano **12**, 4055 (2018).

[23] X. Zhuo, J. Lai, P. Yu, Z. Yu, J. Ma, W. Lu, M. Liu, Z. Liu, and D. Sun, Dynamical evolution of anisotropic response of type-II Weyl semimetal $TaIrTe_4$ under ultrafast photoexcitation, Light Sci. Appl. **10**, 101 (2021).

[24] X. Zhang, N. Mao, O. Janson, J. van den Brink, and R. Ray, Layer dependent topological phases and transitions in $TaRhTe_4$: From monolayer and bilayer to bulk, Phys. Rev. Mater. **8**, 094201 (2024).

[25] M. Behnami, M. Gillig, A. G. Moghaddam, D. V. Efremov, G. Shipunov, B. R. Piening, I. V. Morozov, S. Aswartham, J. Dufouleur, K. Ochkan *et al.*, Large Nernst effect in Te-based van der Waals materials, Phys. Rev. Res. **7**, 023009 (2025).

[26] G. Shipunov, B. R. Piening, C. Wuttke, T. A. Romanova, A. V. Sadakov, O. A. Sobolevskiy, E. Yu Guzovsky, A. S. Usoltsev, V. M. Pudalov, D. V. Efremov *et al.*, Layered van der Waals topological metals of TaTmTe$_4$ (Tm = Ir, Rh, Ru) family, J. Phys. Chem. Lett. **12**, 6730 (2021).

[27] See Supplemental Material at https://link.aps.org/supplemental/10.1103/n7lw-7xqj for magnetotransport properties of TaIrTe$_4$ compound, magnetoconductivity results for the second sample of TaRhTe$_4$, magnetoresistance measurements on additional samples of TaRhTe$_4$, and estimation of the weak localization.

[28] A. A. Burkov, Topological semimetals, Nat. Mater. **15**, 1145 (2016).

[29] G. Sharma, P. Goswami, and S. Tewari, Chiral anomaly and longitudinal magnetotransport in type-II Weyl semimetals, Phys. Rev. B **96**, 045112 (2017).

[30] B. L. Altshuler, D. Khmel'Nitzkii, A. I. Larkin, and P. A. Lee, Magnetoresistance and Hall effect in a disordered two-dimensional electron gas, Phys. Rev. B **22**, 5142 (1980).

[31] P. A. Lee and T. V. Ramakrishnan, Disordered electronic systems, Rev. Mod. Phys. **57**, 287 (1985).

[32] T. Qu, M. Masseroni, T. Taniguchi, K. Watanabe, B. Özyilmaz, T. Ihn, and K. Ensslin, Observation of weak localization in dual-gated bilayer MoS_2, Phys. Rev. Res. **6**, 013216 (2024).

[33] S. Sykora, J. Schoop, L. Graf, G. Shipunov, I. V. Morozov, S. Aswartham, B. Büchner, C. Hess, R. Giraud, and J. Dufouleur, Disorder-induced coupling of Weyl nodes in WTe_2, Phys. Rev. Res. **2**, 033041 (2020).

[34] F. Caglieris, M. Behnami, H. Reichlova, and I. Pallecchi, Chiral anomaly in the Weyl semimetal TaRhTe$_4$ (Data) [Data set], Zenodo (2024), https://doi.org/10.5281/zenodo.14444839.